Analytical Biochemistry 405 (2010) 1–10

Contents lists available at ScienceDirect

Analytical Biochemistry

journal homepage: www.elsevier.com/locate/yabio

Comparison of label-free biosensing in microplate, microfluidic, and spot-based affinity capture assays

Charles J. Choi [a], Alysia R. Belobraydich [b], Leo L. Chan [a], Patrick C. Mathias [c], Brian T. Cunningham [a,c,*]

[a] Department of Electrical and Computer Engineering, University of Illinois at Urbana–Champaign, Micro and Nanotechnology Laboratory, Urbana, IL 61801, USA
[b] Department of Industrial and Enterprise Systems, University of Illinois at Urbana–Champaign, Micro and Nanotechnology Laboratory, Urbana, IL 61801, USA
[c] Department of Bioengineering, University of Illinois at Urbana–Champaign, Micro and Nanotechnology Laboratory, Urbana, IL 61801, USA

ARTICLE INFO

Article history:
Received 8 February 2010
Received in revised form 27 April 2010
Accepted 2 June 2010
Available online 8 June 2010

Keywords:
Photonic crystal
Label-free biosensor
Microplate
Microfluidic
Spot-based assay
Capture affinity assay

ABSTRACT

Using both experimental assays and fluid-dynamic finite element simulation models, we directly compared the achievable performance limits of four distinct assay configurations for label-free detection of an analyte from a test sample on a biosensor surface. The assay configurations studied in this work included a biosensor incorporated into the bottom surface of a microplate well and a microfluidic channel. For each configuration, we compared assay performance for the scenario in which the entire bottom surface of the fluid-handling vessel is coated with capture ligands with assay performance for the scenario in which the capture ligands are applied in the form of localized spots. As a model system, we used detection of the protein biomarker tumor necrosis factor-alpha (TNF-α) using immobilized TNF-α capture antibody. Results show that the microfluidic assay format dramatically reduces the time required to establish a stable equilibrium. Spot-based assays are advantageous for microplate-based detection for reducing the time required for equilibrium sensor response. The results derived are generally applicable to any label-free biosensor technology and any ligand–analyte system with adjustable variables that include sensor mass density sensitivity, analyte–ligand adsorption/desorption rate constants, immobilized ligand density, flow channel geometry, flow rate, and spot size.

© 2010 Elsevier Inc. All rights reserved.

Label-free biosensors operate through transduction of some intrinsic physical quantity associated with biological analytes that can include small molecules, peptides, proteins, DNA, viral particles, bacteria, or cells [1–6]. Accumulation of analyte on the biosensor surface results in changes in the mass density, dielectric permittivity, or some other physical quantity that can be transduced to a measurable output signal [7]. The resulting signal is a product of the complex interaction involving the chemical equilibrium between an immobilized capture ligand and the detected analyte in which both attachment and detachment occur simultaneously. The sensor output signal is also affected by the mass transfer, which may limit the rate of delivery of analyte molecules to the surface, and the loss of available analyte molecules due to scavenging by surfaces other than those incorporating a sensor. Along with the sensor signal output level, the readout background noise, which determines how large a signal must become to be considered statistically detectable, is an important quantity. In a biological or chemical sensor system, the sensor's scale factor (which transduces the adsorbed analyte quantity to the output signal), the noise characteristics of the detection method, the surface chemical equilibrium, and the mass transfer of analyte to the surface interact together. This interaction determines the assay detection limits, the amount of time required to accumulate a measurable signal, and whether a detectable signal should be achievable at all for a given system.

Label-free biosensors have often been designed to function in the context of a flow cell—a microfluidic channel that brings the analyte solution to the sensor [8–13]. Typically in these systems, the sensor is "activated" with an immobilized capture ligand by flowing a solution through the channel, resulting in accumulation of capture molecules upstream of the sensor region. By providing sufficient concentration of analyte and flow rate, mass transfer limitations on the detection of analyte can be overcome, but for low analyte concentrations, capture molecules in regions other than the detection region will "steal" available molecules before they can be detected.

Recently, several technologies have demonstrated the capability of increasing the throughput of label-free biosensor measurements by incorporating sensors into the wells of standard format microplates [14,15]. Although increasing the number of assays that can be performed in parallel, these systems have finite assay volumes, a finite number of detectable molecules, and generally no flow. In addition, new technologies have demonstrated the capability of

* Corresponding author at: Department of Electrical and Computer Engineering, University of Illinois at Urbana–Champaign, Micro and Nanotechnology Laboratory, Urbana, IL 61801, USA.
E-mail address: bcunning@illinois.edu (B.T. Cunningham).

0003-2697/$ - see front matter © 2010 Elsevier Inc. All rights reserved.
doi:10.1016/j.ab.2010.06.009

high spectral resolution molecular detection employing ultra high Q-factor resonators [16,17] and of high-resolution imaging detection, in some cases with the ability to also provide kinetic information on binding [14,18–21] or implementation of arrays of individual sensors on a chip [22–25]. For these technologies, capture ligands are placed in an array of discrete regions of the active biosensor surface or on discrete sensors in the form of nanoliter–picoliter volume droplets using technologies capable of performing accurate droplet deposition using physical contact with metal pins, piezo electric dispensers, and acoustic droplet ejection [26]. In comparison with methods that involve coating the entire inner surfaces of a microplate well or flow channel with capture ligand, spot-based assays can potentially reduce loss of analyte molecules to unwanted surfaces, thereby serving to concentrate detected molecules on the biosensor active area. Therefore, spot-based methods are expected to provide benefits in achievable detection limits.

Detection of trace quantities of biological analytes by a label-free detection system involves a large number of experimental variables and system design parameters. In the design of an assay, it would be valuable to be able to make accurate analytical or numerical predictions on the magnitude of a measured signal, the evolution of a signal over time, and the conditions under which signals will exceed system noise limits. Our goal, therefore, was to develop a comprehensive physical model for a general label-free biosensor system that includes the liquid-handling system as an integral part of the model, taking into account the effects of surfaces with which the analyte solution comes into contact. Although the model shown in this work is applicable to any label-free biosensor, we sought to use a single label-free detection platform, the photonic crystal (PC)[1] biosensor, as a means for comparing the model with experimentally obtained measurements. The PC biosensor is especially advantageous for this purpose because it has been demonstrated in a microplate format [14], a microfluidic format [27–29], and spot-based assays with a high-resolution imaging system [30]. Therefore, the PC biosensors with equivalent performance specifications could be implemented in each of these assay formats for direct comparison. As an example assay, we simulate and demonstrate detection of the protein tumor necrosis factor-alpha (TNF-α) using its capture antibody (anti-TNF-α). Finite element analysis was performed using COMSOL Multiphysics software, which models phenomena defined in different domains in a fully coupled manner.

Materials and methods

PC biosensor

The PC shown in Fig. 1A is a nanostructure composed of a periodically modulated, low refractive index ultraviolet (UV) cured polymer structure coated with a high refractive index dielectric layer of titanium dioxide (TiO_2). The structure is designed to reflect only a narrow band of wavelengths with 100% efficiency when illuminated with white light at normal incidence [31]. The resonant reflection is due to evanescent diffracted orders coupling to modes of an effective high refractive index layer, which are then reradiated through diffraction in-phase with the reflected zero-order wave [32]. A positive shift of the reflected peak wavelength value (PWV) indicates adsorption of material on the sensor surface. Previously, the PC surface has been produced over large surface areas

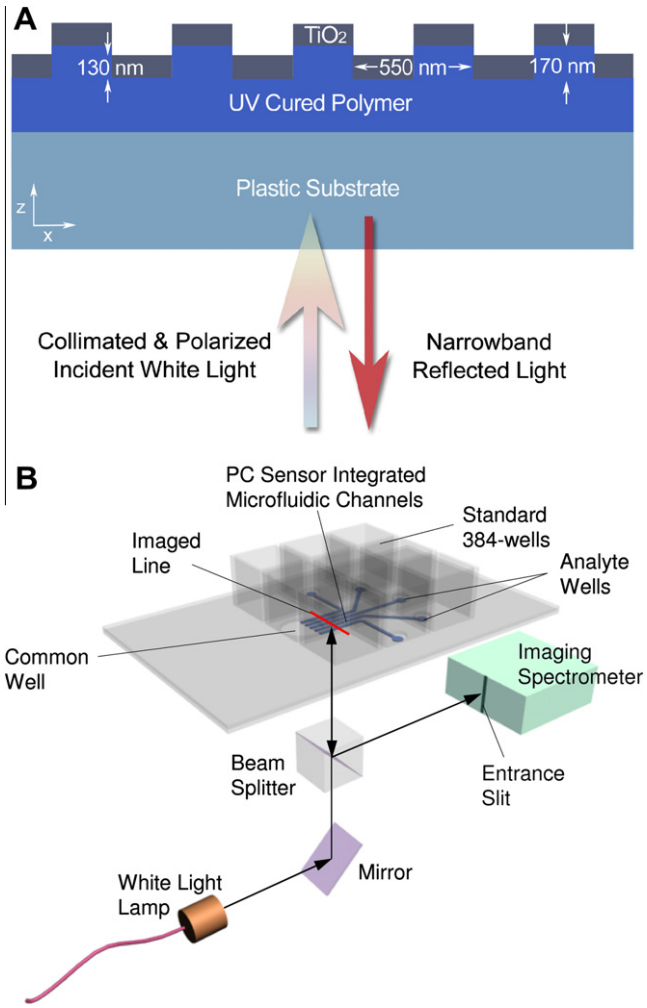

Fig. 1. (A) Schematic cross-section diagram of the PC biosensor. (B) Schematic diagram of the high-resolution imaging detection instrument with PC integrated microfluidic assay chip.

from continuous sheets of plastic film and has been incorporated into standard 96-, 384-, and 1536-well microplates that enable high-throughput assays in a single-use disposable format [14].

Microfluidic sensor fabrication

A room temperature, low-force replica-molding process using a patterned silicon master and a UV curable polymer (Gelest) was used to fabricate the sensor devices [27]. The fabrication method accurately produces submicron features for the PC structure while at the same time generating greater than 10-μm features for the microfluidic channels in a single molding step. First, a silicon wafer was patterned with a 550-nm period one-dimensional (1-D) linear grating structure using deep-UV lithography and reactive ion etching to a depth of 170 nm. The fluid channels were then patterned onto the same silicon wafer using conventional contact lithography and deep reactive ion etching to a depth of 30 μm. As a result of the above processing steps, a negative pattern template of microfluidic channels incorporating a submicron linear grating was fabricated. The completed silicon master was subsequently treated with dimethyl dichlorosilane (GE Healthcare) to promote clean release of the replica from the master.

Next, the master wafer pattern was replicated onto a 250-μm-thick flexible polyethylene terephthalate (PET) substrate (plastic substrate in Fig. 1A) by distributing a layer of liquid UV curable polymer between the silicon wafer and the PET substrate where

[1] *Abbreviations used:* PC, photonic crystal; TNF-α, tumor necrosis factor–alpha; UV, ultraviolet; PWV, peak wavelength value; TiO_2, titanium dioxide; 1-D, one-dimensional; PET, polyethylene terephthalate; SEM, scanning electron microscope; 2-D, two-dimensional; CCD, charge-coupled device; PBS, phosphate-buffered saline; DI, deionized; QCM, quartz crystal microbalance; FEM, finite element method; 3-D, three-dimensional.

the liquid polymer conforms to the shape of the features on the wafer. The liquid polymer was then cured to a solid state by exposure to UV light at room temperature and was subsequently released from the wafer by peeling away the PET, resulting in a polymer replica of the silicon wafer structure adhered to the PET sheet. The sensor structure was completed by depositing 130 nm of TiO_2 on the replica surface using electron beam evaporation. Scanning electron microscope (SEM) images of the PC sensor integrated microchannels can be found in previous publications [27,28]. Anti-TNF-α immobilization surface chemistry (described in the "Assay methods" section next page) was then performed on the open microfluidic channels before sealing with a top PET layer and packaging.

After the TNF-α antibody immobilization, the open microfluidic channels were sealed by a separate PET sheet that had die-punched 1.6-mm-diameter inlet/outlet holes in a pattern corresponding to the locations of the wells of a standard 384-well microplate. The PET cover sheet was bonded using a layer of double-sided, optically clear laminating adhesive film (3 M). To complete the packaging, the fabricated polymer microfluidic network assembly was then attached to a bottomless 384-well microplate using a double-sided adhesive (3 M).

Optical fiber probe instrument

For the standard microplate-based bioassay with the entire bottom surface immobilized with capture antibody, a BIND Reader instrument (SRU Biosystems) was used to illuminate the sensor and to detect the reflected signal [14]. To excite the reflected resonance, a broadband near-infrared light-emitting diode illuminates an approximately 2-mm diameter region of the sensor surface through a 400-μm-diameter optical fiber and a collimating lens at normal incidence through the bottom of the microplate. A detection fiber for gathering reflected light is bundled with the illumination fiber for analysis with a spectrometer. A series of eight illumination/detection heads are arranged in a linear fashion so that reflection spectra are gathered from eight wells in a microplate column at once. The microplate sits on a motion stage so that each column can be addressed in sequence. The instrument is capable of measuring 96 wells in 15 s, although more rapid kinetic information can be gathered from a subset of the plate by measuring a single column at 0.5-s intervals.

Imaging instrument

For microfluidic-based assays and spot-based microplate assays where PWV shifts of small local features on the sensor surface need to be measured, the optical fiber probe system described above cannot be used because its illumination spot size is 2 mm in diameter. Instead, an instrument that is capable of measuring PWV shifts with high spatial resolution, shown in Fig. 1B, is required. In this detection instrument, white light from a tungsten lamp illuminates the sensor at normal incidence with electric field polarization perpendicular to the sensor grating lines. The light reflected from the sensor is directed through a beam splitter to an imaging lens. The light then passes through a narrow slit aperture at the input of an imaging spectrometer. Using this method, reflected light is collected from a line on the sensor surface, where the width of the imaged line is determined by the width of the entrance slit of the spectrometer. The imaging spectrometer contains a two-dimensional (2-D) charge-coupled device (CCD) chip (Acton Research) with 2048×512 pixels, where the line image through the slit is divided into 512 pixels and a spectrum with a resolution of 2048 wavelength data points is acquired for each of the 512 pixels imaged. With the spectral measurement range from 830 to 890 nm, the detection instrument sampling interval is 0.0293 nm. On peak-finding analysis of all 512 spectra, the PWV for each of the 512 pixels is determined; thus, a line of 512 pixels is generated for the PWV image of the sensor. Based on the PWV imaging mechanism described above, the detection instrument is capable of operating in two different modes: kinetic and imaging.

For the kinetic mode in this experiment (measuring ΔPWV as a function of time for the microfluidic-based bioassay), a motorized stage positions the sensor so that the image line remains fixed on a single location that intersects five flow channels (see Fig. 1B) while the PWV of the PC is measured continuously as a function of time. The measurement interval can be designated by the software, where the lower limit (~0.2 s/measurement) is determined by the integration time of the CCD chip, data analysis/routing time, and processing load on the computer. For the imaging mode (generating a 2-D spatial PWV image of the sensor for spot-based microplate bioassay), however, the motorized stage translates the sensor in a direction perpendicular to the image line in small increments, constructing a spatial map of the PC PWV. By this technique, a series of lines are assembled into an image through software, and the same location on the sensor surface can be scanned repeatedly. In the current system, the length of the image line is 9.1 mm, as determined by the size of the CCD chip. A large area can be scanned in a serpentine tiled fashion, where the width of a tile is 9.1 mm along the image line direction. The PWV pixel resolution, or the width of the image line for this work, was 22.3 μm. The imaging detection instrument is able to measure reflected spectra from any PC surface regardless of whether the PC is incorporated into microplate wells or flow channels.

Assay configurations

The four assay configurations are illustrated in Fig. 2, where the schematics in the figure represent a view of the devices from above

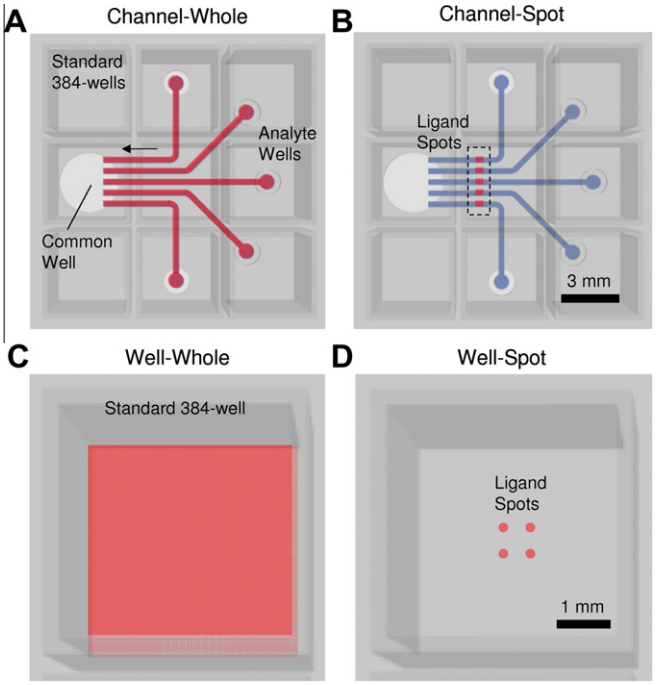

Fig. 2. Schematic diagram of the assay configurations. The areas highlighted in red indicate regions where capture antibodies are immobilized. (A) Microfluidic sensor with entire bottom surface immobilized with capture antibody (channel–whole). The arrow indicates the direction of fluid flow during the analyte binding step. (B) Microfluidic sensor with localized ligand immobilization (channel–spot). (C) Standard 384-well microplate device with entire bottom surface immobilized with ligand (well–whole). (D) Standard 384-well microplate with four immobilized ligand spots (well–spot). Six 384 wells are displayed in panels (A and B), and one 384 well is displayed in panels (C and D). (For interpretation of the references to color in this figure legend, the reader is referred to the Web version of this article.)

looking down into the wells. The area highlighted in red indicates the region where capture antibodies (ligands) are immobilized. The microfluidic assay with capture antibody immobilized on the entire surface of the microchannel walls, which is referred to as "channel–whole," is shown in Fig. 2A, and the microfluidic assay with capture antibodies locally spotted in a 500-μm-wide strip placed on the detection region, which is referred to as "channel–spot," is shown in Fig. 2B. The arrow in Fig. 2A indicates the direction of fluid flow during the analyte binding step. In Fig. 2A and B, six 384 wells are displayed. The standard 384-well microplate assay configuration with the entire bottom surface of the well immobilized with capture antibody, referred to as "well–whole," is shown in Fig. 2C. The assay configuration with four spots of capture antibody (100 μm diameter) placed within a single well of a 384-well microplate sensor is shown in Fig. 2D, which is referred to as "well–spot." One 384 well is displayed in Fig. 2C and D.

Assay methods

Reagents

Human TNF-α and biotinylated anti-human TNF-α capture antibody (MAb11) were purchased from BioLegend. Phosphate-buffered saline (PBS), Tween 20, and glutaraldehyde were purchased from Sigma–Aldrich. BioFX milk blocker solution was purchased from BioFX Laboratories. Streptavidin was purchased from Prozyme. Amine polymer was obtained from SRU Biosystems. 3-Glycidoxypropyldimethylethoxysilane was purchased from Gelest.

Surface chemistry

For the microfluidic-based assays (channel–whole and channel–spot), the anti-TNF-α used for the surface chemistry was biotinylated so that it could bind to a layer of streptavidin attached to the sensor surface through a thin amine polymer coating and a bifunctional linker using an immobilization procedure described previously [33]. Initially, the sensor-integrated microfluidic channels were washed by flowing deionized (DI) water solution from the common well into the channels. Next, the microchannels were filled with a 4% amine polymer solution in DI water and incubated at 25 °C for 24 h. After washing the channels with DI water, glutaraldehyde (25% in DI water) was flowed through and incubated at 25 °C for 2.5 h. After washing the channels with DI water again, streptavidin (0.5 mg ml^{-1} in DI water) was filled and incubated at 4 °C for 24 h. The channels were then washed with DI water, followed by PBS conditioning. For the channel–whole device, the anti-TNF-α solution (0.25 mg ml^{-1} in PBS) was placed onto the entire open channel. For the channel–spot device, the anti-TNF-α solution was spotted onto the open channels by a piezo array spotter (PerkinElmer) in a 4 × 30 array with a spot–spot distance of 150 μm and each spot using 300 ± 30 pl of volume. The spot array was then repeated twice in the same location to ensure uniform antibody density across the strip with enough spot volume for sufficient immobilization. The spotting was done inside a closed chamber with humidity control and substrate temperature set to 12 °C. The anti-TNF-α solution on both the channel–whole and channel–spot devices was then incubated at 4 °C for 18 h, followed by a PBS wash to remove unbound excess anti-TNF-α. The 2-D spatial PWV image of the channel–spot device shown in Fig. 3 was obtained by operating the detection instrument in the spatial imaging mode. The PWVs are represented by the color scale ranging from 860 to 865 nm, where the red region represents an area of greater PWV. It can be observed from the image that the localization of the anti-TNF-α immobilization is achieved. After the anti-TNF-α immobilization and wash, the open microfluidic channels were dried and sealed by a separate PET sheet. They were then packaged by attaching to a bottomless 384-well microplate using an adhesive as described in the device fabrication section.

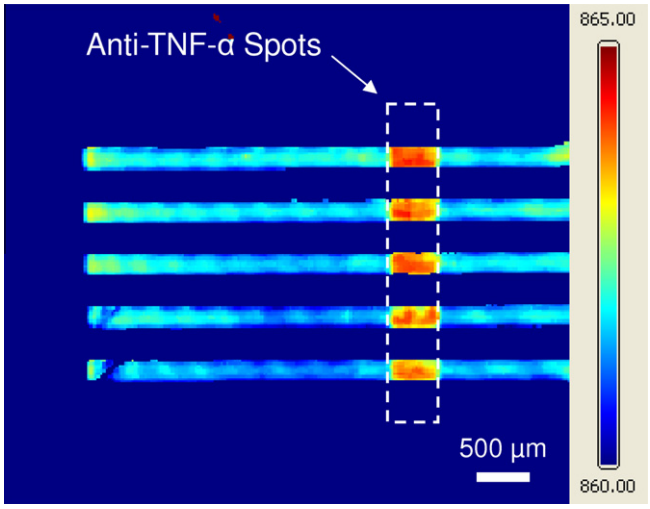

Fig. 3. Two-dimensional spatial PWV image of the microfluidic PC sensor device after spot-based immobilization of anti-TNF-α. The PWVs are represented by the colored scale ranging from 860 to 865 nm, where the red region represents an area of greater PWV. It can be observed from the image that the localization of the anti-TNF-α immobilization is achieved. (For interpretation of the references to color in this figure legend, the reader is referred to the Web version of this article.)

The anti-TNF-α immobilization on the well–whole device was performed using identical reagents and capture antibody surface preparation method as the channel–whole and channel–spot devices. The entire sensor surface on the bottom of the microplate wells were immobilized with anti-TNF-α by pipetting 50 μl of the solution (0.25 mg ml^{-1} in PBS) into each well and incubating for 18 h at 4 °C, followed by PBS wash and a PWV measurement using the optical fiber probe instrument (SRU Biosystems).

The well–spot configuration experiment was performed using a standard PC biosensor microscope slide (1 × 3 inches) and a 384-well size gasket containing a column of 16 wells from SRU Biosystems. The PC biosensor slide was initially surface treated by incubation in an enclosed chamber with 5% 3-glycidoxypropyldimethylethoxysilane in dry toluene at 100 °C overnight. Next, the slide was rinsed with toluene and DI water and then dried with a nitrogen gun. The PC biosensor surface was then spotted with an array of 16 vertical groups of four distinct spots of anti-TNF-α in PBS with 0.01% Tween (assay buffer) at 0.5 mg ml^{-1} and was allowed to bind for 18 h at 4 °C. Epoxysilane-based surface chemistry was used for the well–spot device because a hydrophobic sensor surface was required to prevent the antibody spots from spreading on the sensor surface, particularly along the PC grating lines. The piezo array spotting conditions were identical to those used for the channel–spot device. After the incubation, the gasket was applied to the sensor surface, where each group of the four spots sits in one well. The spots were washed with a large volume of PBS with 2% Tween (wash buffer) and stabilized in 15 μl of PBS with 0.01% Tween, followed by a spatial PWV shift measurement with the imaging instrument operated in the imaging mode.

Binding constant determination

The association and dissociation constants of the TNF-α and anti-TNF-α were determined using the PC integrated microfluidic sensor device through initial rate analysis and dissociation curve fitting, as demonstrated previously [34,35]. TNF-α concentrations of 0.2, 1, 5, and 10 μg ml^{-1} in PBS, and a blank PBS solution as the reference, were introduced into the PC integrated microfluidic chip immobilized with anti-TNF-α on the sensor surface. The wash buffer flow was introduced into the channels 5 min after the introduction of analyte solution so as to observe the dissociation kinet-

ics. Driving fluids to flow through the microchannels during the association/dissociation phase was accomplished by prefilling one or more analyte wells with solution and applying pneumatic pressure. After the analyte wells were prefilled with solution, a silicone cap attached to Teflon micro tubing (Cole–Parmer) was inserted into the opening of the common well and a pressure-regulated lab pneumatic source was used to drive liquid through the channels. Due to the short analyte travel distance, no flow latency among the five microchannels was observed when the analyte solutions were driven through. The anti-TNF-α immobilization protocol for the binding constant determination experiment is identical to the protocol for the microfluidic-based TNF-α assay described in the previous section. The association constant of the TNF-α and anti-TNF-α pair was determined using the initial rate of the sensor response. The dissociation constant was then determined by fitting the dissociation kinetic curves obtained from each of the four analyte channels (one analyte channel was filled with buffer solution) to the solution of the reaction rate equation during the dissociation phase. Using this method, the association constant measured for the TNF-α and anti-TNF-α pair was 0.00727 $(\mu g/ml)^{-1}\,s^{-1}$, and the average dissociation constant measured was $0.0176 \pm 0.00657\ s^{-1}$ (mean ± 1 standard deviation). The kinetic rate constants measured in this experiment yield a binding affinity of $K_d = 0.121 \pm 0.0452$ μM, which is comparable to previously measured values of 0.231 ± 0.542 μM for human TNF-α and anti-human TNF-α monoclonal antibodies obtained with a quartz crystal microbalance (QCM) biosensor [36]. The slight difference in the measured binding affinity with the QCM system is likely due to the use of different types of monoclonal antibodies (Z8 and Z12) and different surface chemistry methods (self-assembled thiol on gold) for immobilizing capture antibodies to the quartz crystal.

Assay procedure

For the microfluidic devices (channel–whole/channel–spot), after the surface chemistry and sealing the open channels, the regions of the channel surface unbound by anti-TNF-α were blocked with 1× concentration BioFX blocking buffer by incubating for 2 h, followed by a PBS wash. After the surface block/wash, TNF-α concentration series of 40, 200, 1000, and 2000 ng ml^{-1} (in PBS) and a blank PBS solution as a negative control were preloaded in each of the analyte wells. Next, data acquisition was initiated with the imaging instrument in the kinetic mode, and the solutions were pumped from each of the analyte wells through the detection area and then to the common well by applying 5 inches Hg of negative pressure at the common well. During the kinetic measurement, the data acquisition line of the imaging instrument was aligned to the center of the localized anti-TNF-α region of the channel–spot device and the same image location was used for the channel–whole device.

For the well–whole device, regions unbound by anti-TNF-α were also blocked with 1× concentration BioFX blocking buffer by incubating in the wells for 2 h, followed by a PBS wash. A range of TNF-α sample concentrations (1, 10, 100, 1000, and 10,000 ng ml^{-1} in PBS), and PBS buffer as a reference, were pipetted into separate wells (50 μl). Kinetic measurement of TNF-α binding for the well–whole device was performed using the optical fiber probe instrument.

As with the previous assay configurations, sensor regions unbound by capture antibodies of the well–spot device were blocked by placing 90 μl of 1× concentration BioFX blocker solution in the wells and incubating for 2 h. After blocker incubation, the wells were washed with a large volume of the wash buffer and stabilized in 15 μl of assay buffer. After stabilization, the sensor surface was scanned with the imaging detection instrument in the spatial imaging mode to obtain a PWV image after blocker immobilization. The TNF-α samples were prepared in a concentration series of 1, 5, 10, 25, 50, 100, 500, 1000, and 5000 ng ml^{-1} in pre-surface-blocked centrifuge tubes. The prepared solutions were pipetted directly into each well (50 μl), including two wells with only an assay buffer as reference wells. The anti-TNF-α spots were allowed to incubate with the TNF-α concentration series overnight at 4 °C. All of the wells were washed with a large volume of wash buffer and stabilized with 15 μl of assay buffer, and a final scan was made with the imaging instrument to obtain a PWV image of TNF-α binding.

Computer simulations

Finite element method (FEM) software (COMSOL) was used to model the kinetic sensor response as analyte molecules in the bulk solution are transported and diffused to bind with the capture molecules available on the sensor surface. The governing differential equation used for the analyte concentration in the bulk solution was the convection diffusion equation listed below as

$$\frac{\partial c}{\partial t} + \nabla \cdot (-D\nabla c + c\vec{u}) = 0, \tag{1}$$

where c, D, and $\vec{u}$ are the bulk analyte concentration, bulk diffusion constant, and fluid flow velocity vector, respectively. For the flow velocity field $\vec{u}$, the parabolic fluid flow velocity profile derived from the incompressible fluid Navier–Stokes equation with no-slip boundary condition was used. At the sensor surface where the ligand–analyte binding reaction occurs, the governing differential equation for the surface-bound analyte concentration used was

$$\frac{\partial c_s}{\partial t} = k_a c(\theta_0 - c_s) - k_d c_s, \tag{2}$$

where c_s is the surface concentration of the analyte bound to the sensor surface, k_a is the association rate constant, k_d is the dissociation rate constant, and θ_0 is the surface concentration of active binding site. At the sensor surface, the boundary condition was represented by coupling of the rate of reaction at the surface with the flux of the reacting species and the concentration of the adsorbed species and bulk species as

$$\vec{n} \cdot (-D\nabla c + c\vec{u}) = k_a c(\theta_0 - c_s) - k_d c_s. \tag{3}$$

At the inlet of the channel where analyte solution is introduced, the boundary condition used was $c = c_0$ and the boundary conditions for the outlet and the channel wall were $\vec{n} \cdot (-D\nabla c + c\vec{u}) = \vec{n} \cdot c\vec{u}$ and $\vec{n} \cdot (-D\nabla c + c\vec{u}) = 0$, respectively. Fig. 4 shows the mesh used for the FEM simulation of kinetic analyte–ligand binding. A finer mesh was used in the bottom surface region where the highest analyte concentration gradients occurs (analyte molecules in the surface region bind with the surface immobilized ligands). The probe locations for the microfluidic-based sensor were 250 μm from the inlet for the channel–spot device (analyte travel distance to the midpoint of the 500-μm-wide capture antibody strip across the channels) and 5 mm for the channel–whole device (analyte travel distance to the imaging instrument's measurement location from the analyte inlet). For the simulation parameters, association and dissociation rates of $k_a = 0.00727$ $(\mu g/ml)^{-1}\,s^{-1}$ and $k_d = 0.0176 \pm 0.00657\ s^{-1}$ (determined from the binding constant measurement) were used. For the surface density of the capture antibody, 22.5 ng mm^{-2} was used based on the analysis of the spatial PWV scan image after the antibody immobilization, where a surface mass density to PWV shift ratio of 9 pg mm^{-2} per 1 nm PWV shift was used. For the flow velocity within the channel, a parabolic flow profile with maximum velocity of 45 mm s^{-1} was used. This velocity was determined from a three-dimensional (3-D) simulation with a negative pressure of 5 inches Hg applied at the common well.

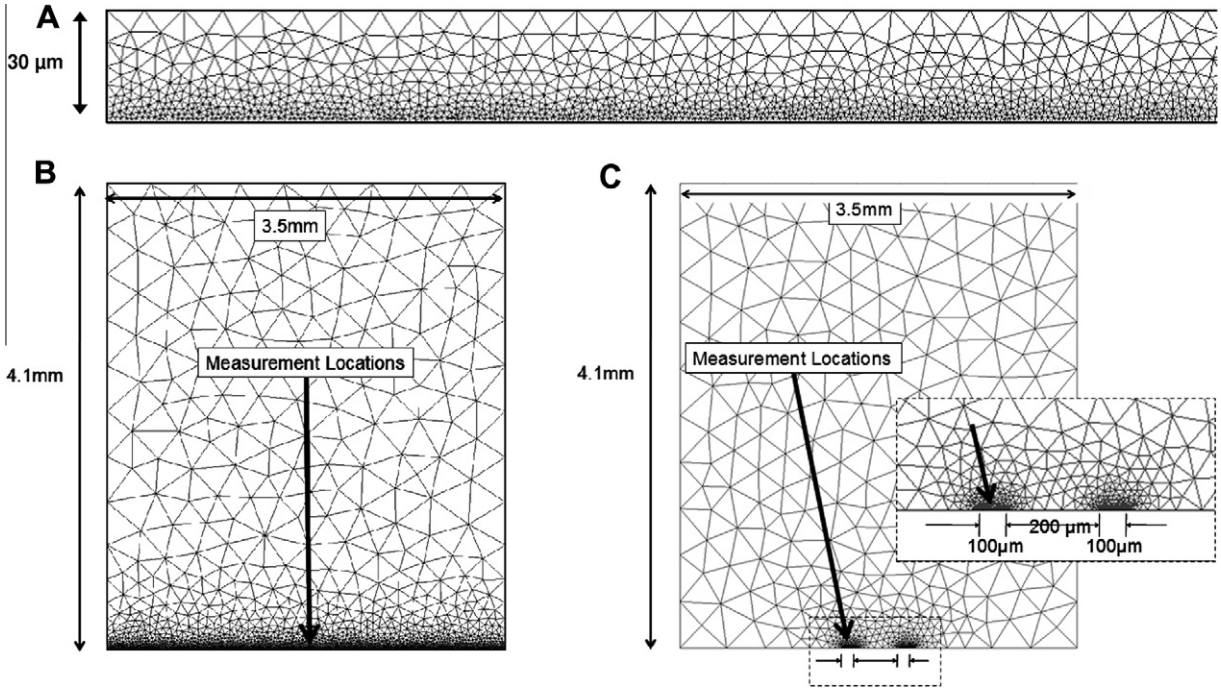

Fig. 4. FEM mesh used for the assay configurations investigated. (A) Microfluidic-based sensor (channel–whole/channel–spot). (B) Microplate sensor with entire bottom surface immobilized with capture antibody (well–whole). (C) Microplate sensor with spotted antibody on the bottom surface (well–spot).

Results: comparison of computer simulations and experimental measurements

The kinetic binding results from the simulation were compared with the experimental measurements. Fig. 5 shows the resulting plots comparing the theoretical and experimental kinetic PWV shift of anti-TNF-α immobilized microfluidic assay chips with the introduction of TNF-α analyte of concentrations ranging from 0.04 to 2 μg ml^{-1}. Fig. 5A and B display the kinetic PWV shift for the channel–whole and channel–spot devices, respectively. The simulation results of the kinetic PWV shift are plotted as thin lines, with dashed lines indicating upper and lower simulated sensor response levels from ±1 standard deviation associated with the measurement of the kinetic dissociation rate, k_d, and the experimental results are plotted in larger circular points. The experimental data in the kinetic PWV shift plots were terminated early compared with the simulation due to the consumption of the TNF-α reagent in the analyte wells. The analyte wells were not refilled with extra TNF-α reagents because the total analyte quantities consumed from the channel-based experiments would be very large for the duration of the experiment to last more than 20 min. This demonstrates the motivation of using the FEM model to predict the response of label-free biosensor without needing to exhaust large quantities of expensive analytes. The differences observed between the theoretical and experimental kinetic shifts could be attributed to the factors that were not included in the FEM model, namely the channel-to-channel variability from the fabrication process, nonuniformities in the capture antibody immobilization density between the channels, and nonspecific binding that may still occur in the regions of the channels with no capture molecules despite the blocking step. The factors mentioned above would also cause the difference in the agreement between theory and experiment for different analyte concentrations and the difference in the agreement observed for the channel–spot device compared with the channel–whole device. Nonetheless, close general agreement was observed between the computer modeled sensor response and the experimentally measured sensor output for both the magnitude of the wavelength shift and the rate of response without the use of any parameters in the computer model that were not determined experimentally.

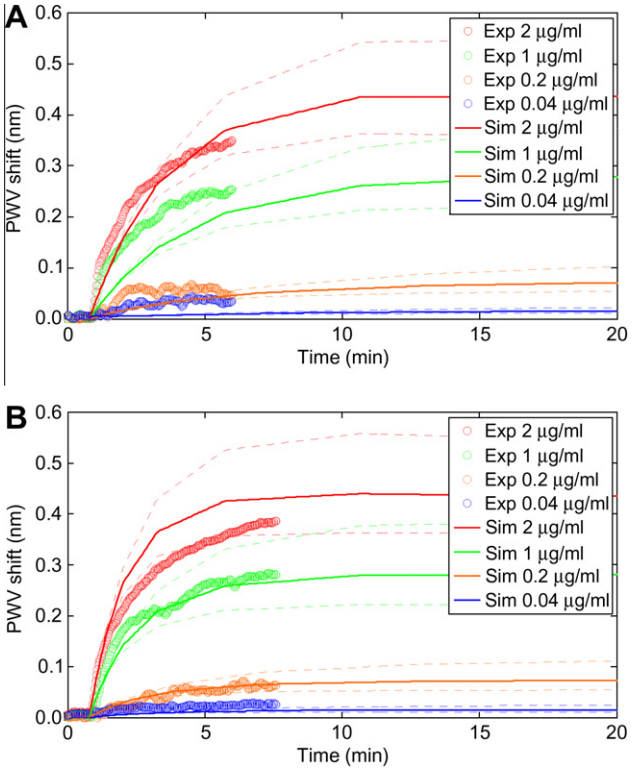

Fig. 5. Theoretical (Sim) and experimental (Exp) comparison of kinetic PWV shift of anti-TNF-α immobilized microfluidic assay chip with introduction of TNF-α analyte of concentrations ranging from 0.04 to 2 μg ml^{-1}: (A) channel–whole; (B) channel–spot.

Fig. 6 shows the theoretical and experimental comparison of kinetic PWV shift of the well–whole device, where TNF-α analyte with concentrations ranging from 0.01 to 10 μg ml^{-1} was used. Again, the simulation results of the kinetic PWV shift are plotted as thin lines, with dashed lines indicating upper and lower simulated sensor response levels from ±1 standard deviation associated with the measurement of the kinetic dissociation rate, k_d, and the experimental results are plotted in larger circular points. As with the results for the microfluidic-based devices, the simulation and experimental results exhibited similar trends without the use of any artificial scaling parameters in the computer model. For the well–whole device, the discrepancies in the kinetic binding curves can be attributed mainly to the fact that the analyte solution in the well was modeled in the simulation as being completely stagnant. In the actual experiment, fluid motion was introduced during the initial analyte reagent introduction through a pipette leading to rapid analyte convection to the antibody immobilized surface, indicated by a consistently higher initial analyte binding rate observed in the experiment. Also in the experiment, some capture antibodies were immobilized on the walls of the well along with the bottom surface, resulting in a reduction of the amount of analyte available for binding compared with that predicted by the model. As with the microfluidic-based sensors, nonspecific binding on the regions not immobilized with capture antibodies can affect the binding kinetics.

For the well–spot device, TNF-α binding measurements were made using the high-resolution imaging detection instrument operated in the spatial imaging mode. Therefore, the PWV shift data from the analyte binding were obtained as endpoints rather than as kinetic plots due to the extensive time required to scan through the PC slide at high spatial resolution. The endpoint PWV shifts of the capture antibody immobilized spots were calculated by considering the PWV shift of pixels in the spot region (active ligand spot), as compared with the PWV shift of regions adjacent to the spots (reference region), before and after injection of TNF-α. Thus, the endpoint PWV shift produced by TNF-α binding to the anti-TNF-α spots was obtained by measuring the PWV shift on the active ligand spot before and after the analyte introduction subtracted from the PWV shift on the reference region before and after the analyte introduction. The analysis method described above can be expressed by the following equation:

$$PWV_{\text{endpoint}} = (PWV_{\text{after}} - PWV_{\text{before}})_{\text{active}} - (PWV_{\text{after}} - PWV_{\text{before}})_{\text{reference}}. \quad (4)$$

This calculation was applied to each of the four spots in each well, and the average of the four spots was taken to obtain the final PWV endpoint value for each TNF-α concentration. The simulated PWV endpoint values, along with the resulting experimental PWV shift endpoint values as a function of the TNF-α analyte concentration, are plotted in Fig. 7. The blue bar represents the computer simulation prediction of the PWV shift endpoint, and the red bar represents the endpoint PWV shift obtained experimentally. The experimental PWV shift values and the simulated PWV shift values showed general agreement, exhibiting the same trend. For lower analyte concentrations, larger percentage coefficient of variation (CV) values associated with lower sensor response levels should be considered for the comparison between the FEM simulation and the experiment. The consistently higher PWV shift for the experimental values can be attributed to the slightly higher level of TNF-α antibody activity in the active region from the epoxysilane-based surface chemistry. The standard deviation values associated with the experimental endpoint PWV shift plot, represented by the error bars, are mainly from the piezo array ligand spot-to-spot variability existing with the four spots within the well for each TNF-α analyte concentration. The error bars for the simulated endpoint PWV shift plot represent upper and lower shift levels from ±1 standard deviation associated with the measurement of the kinetic dissociation rate, k_d.

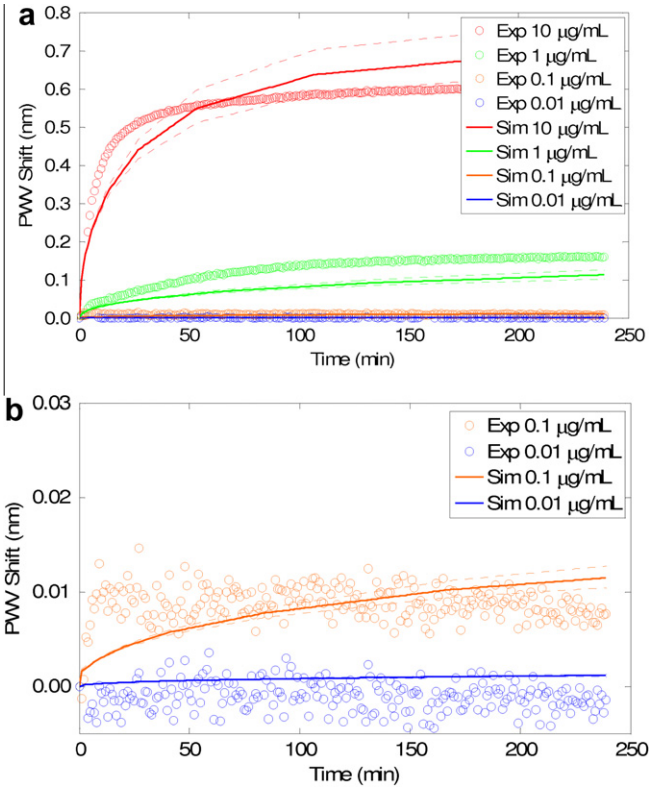

Fig. 6. (A) Theoretical (Sim) and experimental (Exp) comparison of kinetic PWV shift of a well–whole device for TNF-α concentrations ranging from 0.01 to 10 μg ml^{-1}. (B) Kinetic PWV shift for TNF-α concentrations of 0.01 and 0.1 μg ml^{-1}.

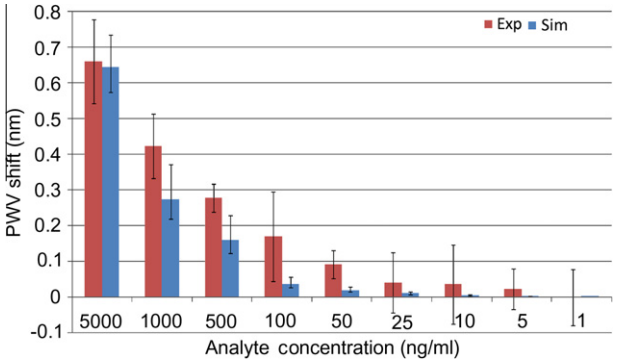

Fig. 7. Theoretical (Sim) and experimental (Exp) comparison of endpoint PWV shift of a well–spot format. The blue bar represents theoretical endpoint PWV shift obtained from FEM simulation, and the red bar represents endpoint PWV shift obtained experimentally. (For interpretation of the references to color in this figure legend, the reader is referred to the Web version of this article.)

Discussion

With the validation of the simulation results through comparison with experimental measurements, the simulation results can be used to obtain predictions of molecular binding interactions in various circumstances. The abilities to predict the magnitude of a sensor response signal, the kinetics of the sensor signal (evolution of the signal over time), and the conditions under which signals

will exceed system noise limits are extremely valuable. Such capabilities are especially valuable for assays that are difficult to perform experimentally or for assays that must run for long durations. Therefore, with the simulation model, the outcome of the bioassay can be predicted at a significantly lower cost without consuming reagents that may be expensive or available only in small quantities. The binding kinetics model was used to examine the equilibrium PWV shift, to compare the amounts of time required to reach equilibrium, and to investigate the detection limit for the four different bioassay configurations. The equilibrium PWV shift values obtained from the simulation of the four different assay platforms are shown in Fig. 8. From the plot, it can be observed that the equilibrium PWV shifts for the channel–whole and channel–spot devices yielded the highest PWV shifts with identical equilibrium PWV shift amounts for both configurations. The well–spot sensor yielded a slightly lower PWV shift that is comparable to the microchannel-based sensors, and the well–whole device produced the lowest level of PWV shift. Comparing the assay conditions for the four configurations, the analyte sample was continuously replenished for the channel–whole/channel–spot devices and the amount of analyte volume relative to the ligand spot area was significantly larger for the well–spot device compared with the well–whole device. Therefore, higher levels of PWV shifts observed in the channel–whole, channel–spot, and well–spot devices are due to the assay condition in which more analyte molecules are available for binding compared with the case for the well–whole device.

In bioassays, the time to reach equilibrium is important because the assay time directly affects the reagent consumption for flow channel methods. Consideration of assay time is also important for reagents that lose activity when exposed to room temperature for extended periods of time. The plot for the time required to reach within 5% of the endpoint equilibrium value with respect to the analyte concentration for different assay configurations is shown in Fig. 9. Comparing the time required to reach equilibrium for all devices, the channel–whole/channel–spot devices reached equilibrium significantly faster than the well–whole/well–spot devices. This is consistent with the assay condition difference in which the well–whole/well–spot assays were run without an active flow, resulting in a biosensor response rate that is limited by the rate of diffusion of TNF-α molecules to the bottom surface of the microplate well. In comparing the microplate-based devices, the well–spot device reached equilibrium faster than the well–whole device. Between the microfluidic-based assays, the time required to reach equilibrium for the channel–spot device was less than that required for the channel–whole device.

It should be noted that the equilibrium PWV shift value does not necessarily reflect the biosensor's ability to measure analyte

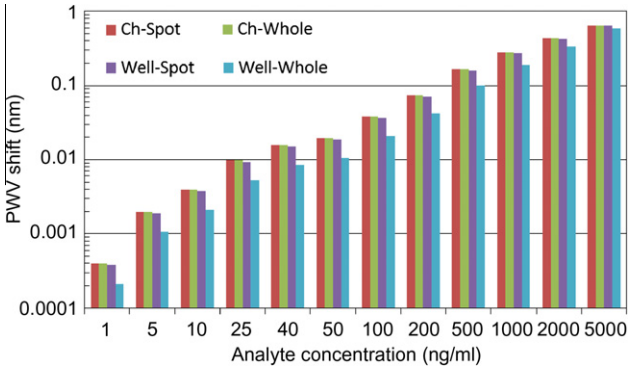

Fig. 8. Simulation results of final equilibrium PWV shifts of anti-TNF-α immobilized sensors for exposure to TNF-α concentrations ranging from 1 to 5000 ng ml^{-1}. Ch, channel.

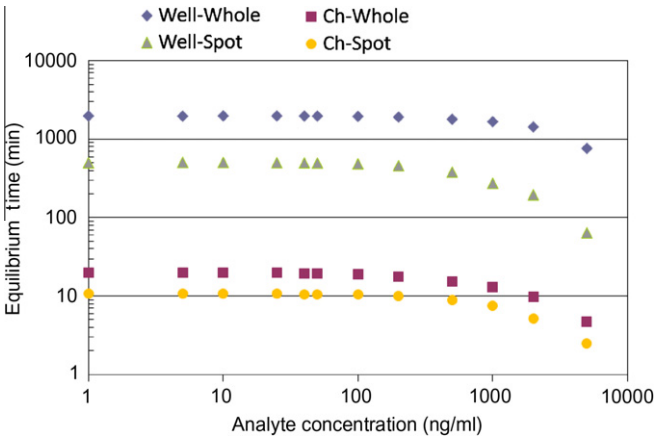

Fig. 9. Simulation results of time required to reach 5% within the equilibrium PWV shift for all assay configurations. Ch, channel.

at low concentrations (limit of detection). Both the standard deviation of the PWV signal of the sensor measurement and the equilibrium PWV shift information need to be considered to obtain the limit of detection. With the PWV measurement setup used here, the standard deviations of the PWV signal measured were $\sigma = 0.00220$ nm for the channel–whole/channel–spot devices (imaging instrument in kinetic mode), $\sigma = 0.00601$ nm for the well–spot device (imaging instrument in spatial imaging mode), and $\sigma = 0.00203$ nm for the well–whole device (fiber-optic probe instrument). The difference in the standard deviation of the PWV signal is due to different measurement setups and methods employed in each case (different probe area and averaging methods). Based on the dose–response curve and the sensor readout noise threshold values (3σ), the limits of detection for the sensors are 16.7 ng ml^{-1} for the channel–whole and channel–spot formats, 48.4 ng ml^{-1} for the well–spot format, and 30.9 ng ml^{-1} for the well–whole format.

For this work, the channel–spot device offers the fastest detection time with low probe molecule use. It also provides the lowest detection limit compared with the well–spot/well–whole devices and has the added capability to measure kinetic rate constants of biomolecular interactions. Compared with the channel–spot format, the channel–whole format offers similar advantages and the same detection limit, but a longer detection time is required. However, the channel–whole format provides the advantage of a simpler assay protocol than the channel–spot device because the added equipment for dispensing reagents at specific locations is not required. On the other hand, for the well–spot format, the imaging instrument operating in the spatial imaging mode, which had the highest sensor signal standard deviation, was used to measure the PWV shift. Therefore, despite its equilibrium level being comparable to the levels of the channel–whole/channel–spot devices and higher than the level of the well–whole device, the limit of detection for the well–spot device is higher and the time required to reach the detection threshold level is longer. However, an advantage of the well–spot format is that probe molecule use is lowest, making it suitable for assays that involve very expensive antibody reagents that are available only in small quantities. The assay format also has the potential to achieve a lower limit of detection with improvements in the sensor readout noise level. Although the detection times are significantly slower compared with the channel–whole/channel–spot devices, the well–whole/well–spot devices offer advantages in terms of analyte reagent consumption because the reagent use in the microplate devices is significantly lower because a continuous flow of reagents is not required. In comparing the well–whole and well–spot configurations, the well–whole format offers a simpler assay protocol and

Table 1
Comparison of PC label-free assay formats.

	Channel–whole	Channel–spot	Well–whole	Well–spot
Instrument resolution (nm)	0.0066	0.0066	0.0061	0.018
Detection limit (ng/ml)	16.7	16.7	30.9	48.4
Equilibrium response for 50 ng/ml TNF-α (nm)	0.0195	0.0195	0.0105	0.0186
Time required to reach equilibrium for 50 ng/ml TNF-α (min)	19.3	10.60	1965	498
Advantages	Fast detection Largest PWV shift Lowest detection limit Binding constants measurable	Fastest detection Largest PWV shift Lowest detection limit Binding constants measurable	Low analyte consumption Simple assay protocol	Low analyte consumption Lowest ligand consumption
Disadvantages	Large analyte consumption[a]	Large analyte consumption[a] Complex assay protocol	Smaller PWV shift Large ligand consumption	Complex assay protocol

[a] Analyte consumption could be the lowest for applications where sensor response level is high and measurement time is not of an issue.

the detection limit is lower with the current measurement setup. For this work, it should be noted that for applications that have high sensor response levels, or where the sensor measurement response time is not an issue, microfluidic-based devices do not require consumption of large quantities of reagents in comparison with the microplate format. A comparison of the four assay formats investigated in this work is shown in Table 1.

Conclusion

In this work, we have investigated four different combinations of bioassay formats and capture molecule immobilization methods through the use of label-free PC biosensors. The assay platforms investigated were a PC biosensor integrated microfluidic device with capture antibody spots immobilized local to the detection area (channel–spot), a microfluidic sensor device with the entire surface immobilized with capture antibodies (channel–whole), a standard 384-well microplate-based PC biosensor with capture antibody spots in the well (well–spot), and the same 384-well microplate sensor with the entire bottom surface immobilized with capture antibodies (well–whole). FEM simulation was used to model the biomolecular binding kinetics occurring in the different assay platforms, and the results from the model were verified experimentally through the protein–protein binding affinity assay using TNF-α and anti-TNF-α. The simulation model was then used to predict the equilibrium sensor response, the sensor measurement time required to reach the equilibrium levels, and the detection limit of the TNF-α protein binding assay, taking into account the conditions for each of the four assay formats. The results were then used to compare the assay performance for each of the assay methods. The microfluidic-based formats (channel–spot/channel–whole) offered the fastest detection time, the largest equilibrium binding of analyte, and the lowest detection limit. In addition, the reaction rate constants of biomolecular interaction could be measured. The well–spot device offered the lowest amount of ligand consumption with low analyte volume and has the potential for a lower detection limit given that the equilibrium analyte binding level was similar to that of the microfluidic-based formats. The well–whole format offered low analyte consumption with a simple assay protocol. The assay performance results for different platforms obtained in this work are applicable to any label-free biosensor system based on surface detection where analyte molecules are brought into contact with the capture molecule immobilized on the sensor surface.

Acknowledgment

The authors are grateful to Frank Wang (SRU Biosystems) for valuable discussions on the label-free biosensor measurements and to Derek Puff (SRU Biosystems) for writing the software that enabled the kinetic measurements to be performed on the detection instrument. The authors also gratefully acknowledge SRU Biosystems for providing financial support, the staff of the Micro and Nanotechnology Laboratory, and the Center for Nanoscale Chemical–Electrical–Mechanical Manufacturing Systems (Nano-CEMMS) at the University of Illinois at Urbana–Champaign. This material is based on work supported by the National Science Foundation under awards DMI 0328162 and 0427657. Any opinions, findings, and conclusions or recommendations expressed in this material are those of the authors and do not necessarily reflect the views of the National Science Foundation. We disclose that coauthor Brian T. Cunningham is a founder of SRU Biosystems.

References

[1] B. Lin, J. Qiu, J. Gerstenmeier, P. Li, H.M. Pien, J. Pepper, B. Cunningham, A label-free optical technique for detecting small molecule interactions, Biosens. Bioelectron. 17 (2002) 827–834.
[2] K. Maehashi, T. Katsura, K. Kerman, Y. Takamura, K. Matsumoto, E. Tamiya, Label-free protein biosensor based on aptamer-modified carbon nanotube field-effect transistors, Anal. Chem. 79 (2007) 782–787.
[3] B.R. Baker, R.Y. Lai, M.S. Wood, E.H. Doctor, A.J. Heeger, K.W. Plaxco, An electronic, aptamer-based small-molecule sensor for the rapid, label-free detection of cocaine in adulterated samples and biological fluids, J. Am. Chem. Soc. 128 (2006) 3138–3139.
[4] M.F. Pineda, L.L.Y. Chan, T. Kuhlenschmidt, C.J. Choi, M. Kuhlenschmidt, B.T. Cunningham, Rapid specific and label-free detection of porcine rotavirus using photonic crystal biosensors, IEEE Sens. J. 9 (2009) 470–477.
[5] R. Maalouf, C. Fournier-Wirth, J. Coste, H. Chebib, Y. Saikali, O. Vittori, A. Errachid, J.P. Cloarec, C. Martelet, N. Jaffrezic-Renault, Label-free detection of bacteria by electrochemical impedance spectroscopy: comparison to surface plasmon resonance, Anal. Chem. 79 (2007) 4879–4886.
[6] L.L. Chan, S.L. Gosangari, K.L. Watkin, B.T. Cunningham, Label-free imaging of cancer cells using photonic crystal biosensors and application to cytotoxicity screening of a natural compound library, Sens. Actuat. B 132 (2008) 418–425.
[7] M.A. Cooper, Label-free screening of bio-molecular interactions, Anal. Bioanal. Chem. 377 (2003) 834–842.
[8] H.Y. Zhu, I.M. White, J.D. Suter, X.D. Fan, Phage-based label-free biomolecule detection in an opto-fluidic ring resonator, Biosens. Bioelectron. 24 (2008) 461–466.
[9] R.L. Rich, D.G. Myszka, Higher throughput, label-free, real-time molecular interaction analysis, Anal. Biochem. 361 (2007) 1–6.
[10] A.D. Taylor, J. Ladd, Q.M. Yu, S.F. Chen, J. Homola, S.Y. Jiang, Quantitative and simultaneous detection of four foodborne bacterial pathogens with a multi-channel SPR sensor, Biosens. Bioelectron. 22 (2006) 752–758.
[11] C. Barzen, A. Brecht, G. Gauglitz, Optical multiple-analyte immunosensor for water pollution control, Biosens. Bioelectron. 17 (2002) 289–295.
[12] R.W. Glaser, Antigen-antibody binding and mass transport by convection and diffusion to a surface: a 2-dimensional computer model of binding and dissociation kinetics, Anal. Biochem. 213 (1993) 152–161.
[13] P. Schuck, A.P. Minton, Analysis of mass transport-limited binding kinetics in evanescent wave biosensors, Anal. Biochem. 240 (1996) 262–272.
[14] B.T. Cunningham, P. Li, S. Schulz, B. Lin, C. Baird, J. Gerstenmaier, C. Genick, F. Wang, E. Fine, L. Laing, Label-free assays on the BIND system, J. Biomol. Screen. 9 (2004) 481–490.
[15] G.J. Ciambrone, V.F. Liu, D.C. Lin, R.P. McGuinness, G.K. Leung, S. Pitchford, Cellular dielectric spectroscopy: a powerful new approach to label-free cellular analysis, J. Biomol. Screen. 9 (2004) 467–480.

[16] A.M. Armani, R.P. Kulkarni, S.E. Fraser, R.C. Flagan, K.J. Vahala, Label-free, single-molecule detection with optical microcavities, Science 317 (2007) 783–787.
[17] F. Vollmer, S. Arnold, Whispering-gallery-mode biosensing: label-free detection down to single molecules, Nat. Methods 5 (2008) 591–596.
[18] D. Wassaf, G.N. Kuang, K. Kopacz, Q.L. Wu, Q. Nguyen, M. Toews, J. Cosic, J. Jacques, S. Wiltshire, J. Lambert, C.C. Pazmany, S. Hogan, R.C. Ladner, A.E. Nixon, D.J. Sexton, High-throughput affinity ranking of antibodies using surface plasmon resonance microarrays, Anal. Biochem. 351 (2006) 241–253.
[19] E. Ozkumur, J.W. Needham, D.A. Bergstein, R. Gonzalez, M. Cabodi, J.M. Gershoni, B.B. Goldberg, M.S. Unlu, Label-free and dynamic detection of biomolecular interactions for high-throughput microarray applications, Proc. Natl. Acad. Sci. USA 105 (2008) 7988–7992.
[20] M. Zhao, X.F. Wang, D.D. Nolte, Molecular interferometric imaging, Optics Express 16 (2008) 7102–7118.
[21] R.L. Rich, M.J. Cannon, J. Jenkins, P. Pandian, S. Sundaram, R. Magyar, J. Brockman, J. Lambert, D.G. Myszka, Extracting kinetic rate constants from surface plasmon resonance array systems, Anal. Biochem. 373 (2008) 112–120.
[22] R. McKendry, J.Y. Zhang, Y. Arntz, T. Strunz, M. Hegner, H.P. Lang, M.K. Baller, U. Certa, E. Meyer, H.J. Guntherodt, C. Gerber, Multiple label-free biodetection and quantitative DNA-binding assays on a nanomechanical cantilever array, Proc. Natl. Acad. Sci. USA 99 (2002) 9783–9788.
[23] Z.Q. Gao, A. Agarwal, A.D. Trigg, N. Singh, C. Fang, C.H. Tung, Y. Fan, K.D. Buddharaju, J.M. Kong, Silicon nanowire arrays for label-free detection of DNA, Anal. Chem. 79 (2007) 3291–3297.
[24] A.L. Washburn, L.C. Gunn, R.C. Bailey, Label-free quantitation of a cancer biomarker in complex media using silicon photonic microring resonators, Anal. Chem. 81 (2009) 9499–9506.
[25] S. Mandal, D. Erickson, Nanoscale optofluidic sensor arrays, Optics Express 16 (2008) 1623–1631.
[26] I. Barbulovic-Nad, M. Lucente, Y. Sun, M.J. Zhang, A.R. Wheeler, M. Bussmann, Bio-microarray fabrication techniques: a review, Crit. Rev. Biotechnol. 26 (2006) 237–259.
[27] C.J. Choi, B.T. Cunningham, Single-step fabrication and characterization of photonic crystal biosensors with polymer microfluidic channels, Lab. Chip. 6 (2006) 1373–1380.
[28] C.J. Choi, B.T. Cunningham, A 96-well microplate incorporating a replica molded microfluidic network integrated with photonic crystal biosensors for high throughput kinetic biomolecular interaction analysis, Lab. Chip. 7 (2007) 550–556.
[29] B.R. Schudel, C.J. Choi, B.T. Cunningham, P.J.A. Kenis, Microfluidic chip for combinatorial mixing and screening of assays, Lab. Chip. 9 (2009) 1676–1680.
[30] L.L. Chan, B.T. Cunningham, P.Y. Li, D. Puff, A self-referencing method for microplate label-free photonic-crystal biosensors, IEEE Sens. J. 6 (2006) 1551–1556.
[31] R. Magnusson, S.S. Wang, New principle for optical filters, Appl. Phys. Lett. 61 (1992) 1022–1024.
[32] D. Rosenblatt, A. Sharon, A.A. Friesem, Resonant grating waveguide structures, IEEE J. Quantum Electron. 33 (1997) 2038–2059.
[33] W. Zhang, N. Ganesh, I.D. Block, B.T. Cunningham, High sensitivity photonic crystal biosensor incorporating nanorod structures for enhanced surface area, Sens. Actuat. B 131 (2008) 279–284.
[34] C.J. Choi, I.D. Block, B. Bole, D. Dralle, B.T. Cunningham, Label-free photonic crystal biosensor integrated microfluidic chip for determination of kinetic reaction rate constants, IEEE Sens. J. 9 (2009) 1697–1704.
[35] P.R. Edwards, R.J. Leatherbarrow, Determination of association rate constants by an optical biosensor using initial rate analysis, Anal. Biochem. 246 (1997) 1–6.
[36] Y. Liu, W. Zhang, X. Yu, H.W. Zhang, R. Zhao, D. Shangguan, Y. Li, B.F. Shen, G.Q. Liu, Quartz crystal biosensor for real-time kinetic analysis of interaction between human TNF-α and monoclonal antibodies, Sens. Actuat. B 99 (2004) 416–424.